Energy Conversion and Management 283 (2023) 116948

Contents lists available at ScienceDirect

Energy Conversion and Management

journal homepage: www.elsevier.com/locate/enconman

Novel battery thermal management via scalable dew-point evaporative cooling

Jie Lin [a,b,c,*], Howie N. Chu [b], Kyaw Thu [d], Malgorzata Wojtala [b], Fei Gao [e], Kian Jon Chua [c]

[a] Department of Chemical Engineering, University College London, Gower Street, London WC1E, 6BT, United Kingdom
[b] Department of Engineering Science, University of Oxford, Parks Road, Oxford OX1 3PJ, United Kingdom
[c] Department of Mechanical Engineering, National University of Singapore, 9 Engineering Drive 1, Singapore 117575, Singapore
[d] Interdisciplinary Graduate Schools of Engineering Science, Kyushu University, Kasuga-koen 6-1, Kasuga-shi, Fukuoka 816-8580, Japan
[e] Department of Electrical Engineering, Shanghai Jiao Tong University, 800 Dongchuan Road, Shanghai 200240, China

ARTICLE INFO

Keywords:
Active battery cooling
Air cooling
Dew-point evaporative cooling
Electrochemical-thermal modeling
Battery thermal characterization

ABSTRACT

Thermal management is critical to safety, stability, and durability of battery energy storage systems. Existing passive and active air cooling are not competent when the cooling performance, energy efficiency and cost of the thermal management system are drawing concurrent concerns. Here we propose dew-point evaporative cooling as a novel active air-cooling approach for large battery systems. Its capability of cooling the air towards its dew-point temperature with simple working principle and great electrical efficiency offers an ideal solution. Therefore, a scalable dew-point evaporative cooling technology was developed, and a large-scale cooler was constructed which could deliver 2.9–6.7 kW cooling capacity with 8.9–28.9 coefficient of performance (COP). To demonstrate its performance for battery thermal management, we took a 20 Ah lithium iron phosphate (LFP) prismatic pouch cells for a case study whose complex dynamic electrochemical and thermal responses were investigated via lock-in thermography experiments and electrochemical-thermal modeling. The potential of dew-point evaporative cooling for battery cooling was explored via the multi-physics coupling of battery and cooler models. This study elucidates that dew-point evaporative cooling can efficiently cool a battery by 3.0–13.6 °C lower than the cases with only forced convection, and control the battery operating temperature within an ideal operating range of 20–40 °C.

1. Introduction

The climate change arising from excessive carbon emissions has posed a serious threat to almost everything in the world, including creature, food, water, environment, and economy [1]. This emphasizes the obligation of next energy revolution from fossil fuel to renewables (solar, wind and tidal energy, etc.) [2]. To alleviate the demand for fossil fuel and to cope with the instability of renewable energy, developing smart grids with electrical energy storage systems seems to be the most promising solution [3]. With great advancements in battery chemistry, energy density, stability and cyclability, lithium-ion battery has become the leading electrical energy storage device in consumer electronics, electric vehicles and grid networks [4].

Battery operation involves complex electrochemical processes [5], such as lithium (de)intercalation, charge transfer, ion diffusion and migration, etc. Owing to the internal electrical and kinetic resistance, as well as battery entropy change, a considerable amount of heat is generated during battery charging and discharging [6]. As battery temperature can severely impact its physicochemical properties (e.g., conductivity, diffusivity and reaction rate constant) [7], heat generation in batteries, if not properly dissipated, can alter battery electrochemical performance, accelerate battery degradation and even lead to catastrophic thermal runaway [8]. Hence, thermal management is necessary and forms an essential part of a battery system [9].

In general, battery thermal management requires fast-response and cost-effective solutions that are able to maintain battery temperature within a suitable range (i.e., 20–40 °C) [10]. The most common approaches include conventional air and liquid cooling [11], which employ air or liquids to cool battery packs through convection. Air cooling through passive and active techniques is the simplest way to dissipate heat from batteries, with little electricity consumption to maintain the fluid flows [12]. However, if the supply air is not appropriately pre-cooled or ventilated, it may not be efficient to

* Corresponding author at: Department of Chemical Engineering, University College London, Gower Street, London WC1E, 6BT, United Kingdom.
E-mail addresses: jie.lin@ucl.ac.uk, lin_j@u.nus.edu (J. Lin).

https://doi.org/10.1016/j.enconman.2023.116948
Received 2 November 2022; Received in revised form 20 February 2023; Accepted 16 March 2023
Available online 28 March 2023

Nomenclature

a	specific surface area, m^2/m^3
c	concentration, mol/m^3
c_p	specific heat, J/(kg·K)
COP	coefficient of performance
D	diffusion coefficient, m^2/s
E	activation energy, J/mol
F	Faraday constant, 96,485C/mol
h	heat transfer coefficient, $W/(m^2 \cdot K)$
k	thermal conductivity, W/(m·K)
i	current density, A/m^2
i_0	exchange current density, A/m^2
L	length, mm
N	number of cell layer
$\overrightarrow{N}$	mass flux, $mol/(m^2 \cdot s)$
P	pressure, Pa
Q	cooling capacity, W
$\dot{q}$	heat generation rate, W/m^3
r	radius, μm
R	universal gas constant, 8.314 J/(mol·K)
R_s	particle radius, μm
R_w	working air ratio
Re	Reynolds number
S	specific entropy, J/(mol·K)
t	time, s
T	temperature, K
t_+^0	transference number
u	velocity, m/s
U	potential, V
$\dot{V}$	volumetric flow rate, m^3/s
W	width, mm
$\dot{W}$	power, W

Greek symbols

α	charge transfer coefficient
ε	volume fraction
σ	electrical conductivity, S/m
ϕ	electric potential, V
η	overpotential, V
ρ	density, kg/m^3
μ	dynamic viscosity, Pa·s
ω	humidity ratio, kg/kg
κ	ionic conductivity, S/m
δ	thickness, mm

Superscripts

brug	Bruggeman coefficient
eff	effective

Subscripts

0	initial state
a	air
app	applied current
amb	ambient
avg	average
e	entropic
eq	equilibrium
i	reaction current
j	joule
l	liquid
max	maximum
min	minimum
p	product air
r	reaction
ref	reference
s	solid
su	supply air
surf	surface
v	vapor
w	working air

Abbreviations

CC	current collector
CFD	computational fluid dynamics
DoD	depth of discharge
DPEC	dew-point evaporative cooling
EoD	end of discharge
LFP	lithium iron phosphate
OCP	open circuit potential
P2D/P4D	pseudo-2D/pseudo-4D
PCM	phase change material
RMSE	root-mean-square error
SOC	state of charge

counterbalance the battery heat load. In contrast, liquid cooling usually has larger cooling capacity, which is favored in high-power battery systems with considerable heat generation rate [13]. Heat exchangers with mini- or micro-channels for liquid coolant are subsequently developed to improve the effectiveness of liquid cooling, with higher power consumption as a penalty [14]. In combination with air and liquid cooling, heat pipes, designed to be in direct contact with batteries, have been considered for thermal management [13]. They can effectively transfer heat from batteries to a heat sink and improve temperature uniformity across the batteries [15].

In addition, various kinds of phase change material (PCM) [16,17], such as paraffin wax, stearic acid, polyethylene glycol, and their thermal conductive composites with aluminum foam [18], copper mesh [19] and graphite [20], have been proposed for battery thermal management due to their high capacity to store thermal energy. PCM can absorb a large quantity of heat generated in batteries and its constant melting point can restrict battery peak temperature and improve temperature uniformity. Similarly, novel metal–organic framework sorption material [21] has been tested effective in controlling battery temperature during its desorption/sorption process, which can be coated on the battery surfaces as a thin layer. Although heat pipes, PCM, and sorption materials have shown convincing performance, their passive cooling nature inevitably requires another air or liquid cooling system to dissipate heat stored in them. The total capacity of thermal energy storage material should also be carefully designed to match the heat generation from a specific battery system. A summary of different available battery thermal management approaches is illustrated in Fig. 1.

In this work, we focus on active air cooling which has continued to be a reliable and economical method for thermal management of large-scale battery energy storage systems. An emerging air cooling technology, i.e., dew-point evaporative cooling (DPEC, also called the Maisotsenko cycle) [22], is proposed to control the battery operating temperature. It allows the supply air to be deeply cooled towards its inlet dew point before being used for cooling applications. Earlier research work has been carried out to design and fabricate dew-point evaporative coolers with different flow patterns, such as cross-flow [23], parallel flow [24] and counter-flow [25]. Lumped parameter [26], ε-number of transfer units (NTU) [27], modified log mean temperature difference (LMTD) [28] and computational fluid dynamics (CFD) [29] models have been developed to study their governing heat and mass transfer process.

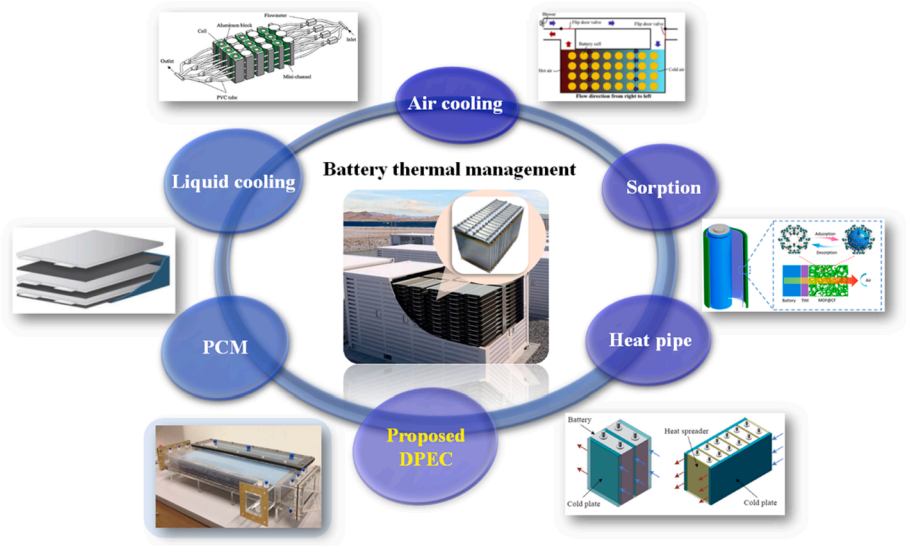

Fig. 1. Summary of different battery thermal management approaches [21,36–39].

Following these efforts, many experimental tests on dew-point evaporative coolers demonstrated competitive cooling effectiveness to conventional mechanical vapor compression chillers [30], and excellent energy efficiency with up to 50 coefficient of performance (COP) could be achieved [31]. Further energy, economic and environmental analyses revealed this cooling approach could achieve great savings in life cycle cost with 3–15 years of payback period and 18 %–30 % reduction in carbon emission, if replacing conventional air-conditioning system [32]. Hence, dew-point evaporative cooling is an ideal solution to cool power electronics [33], data centers [34] and battery systems [35] where intensive sensible heat loads are present and should be properly managed. However, no comprehensive attempt to date has been made to explore the possibility of using dew-point evaporative cooling for battery thermal management.

Herein we manage to develop a scalable dew-point evaporative cooling technology so that coolers from a prototype-scale unit to a kilowatt-scale device can be established, which is a critical step for handling practical battery energy systems. The excellent cooling effectiveness and energy efficiency obtained from the small coolers can be successfully reproduced and remain stable in the upsized cooler. On the other hand, we test a type of large-format 20 Ah lithium–iron-phosphate (LFP) prismatic pouch cells in lock-in thermography experiments with the applied current up to 4C, and a new pseudo-4D (P4D) electrochemical-thermal battery model is established to capture the dynamic cell voltage and temperature responses. The model considers spatial and temporal variations of current flow, charge transfer and lithium diffusion in a full 3D cell geometry, and the consequent locally varying heat generation is projected to a 3D thermal model to account for the important temperature features observed in the thermography tests. We further investigate the potential of the large-scale dew-point evaporative cooler for battery thermal management via forced heat convection. The potential cooling effect that a dew-point evaporative cooler can achieve on the battery electrical and thermal behaviors is examined by a robust multiphysics coupling of the battery and cooler models. We demonstrate that dew-point evaporative cooling can be an effective technique to control battery operating temperature within an appropriate range even at high C-rates (C-rate refers to the inverse of time in hours required to fully charge/discharge the battery based on its nominal capacity). Its high cooling capacity and COP promote itself to be an ideal solution for large battery energy storage systems.

2. Experimental

2.1. Dew-point evaporative cooler

Dew-point evaporative cooling can be widely used to pre-cool the ambient air that is driven to dissipate the intensive heat generation from batteries. An illustration of dew-point evaporative cooling is provided in Fig. 2. A dew-point evaporative cooler is a heat and mass exchanger with dry and wet air channels, and the wet channel surfaces are covered by a water film [40,41]. The ambient air into the cooler will flow through the dry channels where it is cooled by the working air in the adjacent wet channels through water evaporation. At the end of dry channels, a portion of the supply air is directed into wet channels as the working air (secondary air stream) to sustain the evaporative cooling process, while the rest is extracted as the product air (primary air stream) for cooling purpose. The working air usually takes up 30–40 % (defined as working air ratio R_w) of the supply air flow rate [42]. The cooling process utilizes the latent heat transfer during water evaporation to remove the sensible heat from the supply air. Through separation of dry and wet air channels and pre-cooling of the working air, the innovative flow configuration of dew-point evaporative cooling can reduce the supply air temperature towards its inlet dew point.

Multiscale dew-point evaporative coolers have been developed, as shown in Fig. 3(a)-(b). A prototype-scale unit was first made of acrylic sheets, and 200 μm thick polyethylene terephthalate (PET) polymer sheets were selected as the impervious channel plate to separate dry and wet air channels. A type of 200-μm-thick porous natural cellulose fabric was coated on wet channel surfaces as the wick material to absorb and retain a thin water film for evaporative cooling. A water tank was installed at one side of the cooler units and the wick material from wet channels was extended and immersed into the water tank. The prototype-scale unit consists of 10 pairs of dry and wet channels with channel dimensions of 600 × 150 × 3 mm (L × W × H).

The design of small cooler prototypes was further scaled up to a large practical cooler with a rated cooling capacity of 5 kW in Fig. 3(b). The large-scale cooler is comprised of 10 cooler modules of which each is similar to the cooler prototype developed in Fig. 3(a). A cooler module has 20 channel pairs with dimensions of 1000 × 250 × 3 mm and can be easily assembled or dissembled. For mass production of the modules, polyvinyl chloride (PVC) sheets were adopted to replace the original acrylic sheets. A cascaded water tank was installed at the center of the cooler. Water is supplied from the top of the tank and exits at the bottom. The product air outlet is at the back of the cooler and the working air is

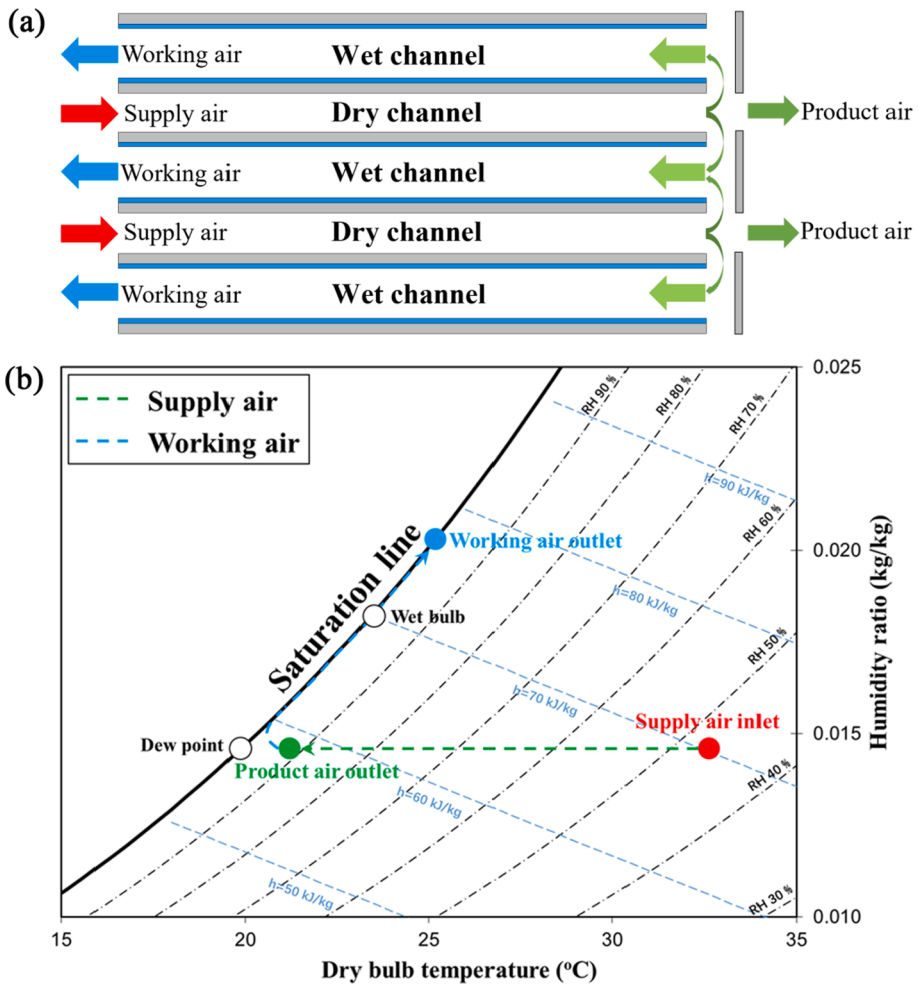

Fig. 2. Working principle of dew-point evaporative cooling. (a) Schematic diagram. (b) Psychrometric chart. The white circles mark the dew-point and wet-bulb temperatures of the inlet air.

exhausted from the top.

A test system was set up for each dew-point evaporative cooler to investigate its thermodynamic performance, as illustrated by the schematic diagram in Fig. 3(c). The dry bulb and wet bulb temperatures of each inlet and outlet air stream were measured by RTD sensors (1/10 DIN, Omega Engineering) to obtain the air psychrometric state. The air flowrates were calculated from air velocity meters (±2.0 % full-scale, Omega Engineering) installed on straight pipes with appropriate diameter and length to ensure steady flows. The air pressure drop at different outlets were measured by differential pressure sensors (±1.0 % full-scale, Omega Engineering). The instant power consumption was recorded by either a portable power meter (±2.0 % full-scale, Energenie) for the cooler prototypes or a wall-mounted power meter (±0.5 % full-scale, IME) for the large-scale cooler. A control and datalogging system was established using the hardware from National Instruments on the Labview interface.

The cooling capacity of dew-point evaporative coolers is calculated from the enthalpy change of the product air before and after the cooler, expressed as

$$Q = \rho_a \dot{V}_p (h_{su} - h_p) = \rho_a \dot{V}_p c_p (T_{su} - T_p) \quad (1)$$

The energy efficiency of the cooler, or COP, is defined as the ratio of the cooling capacity generated by the cooler to its electrical power consumption, as shown below

$$\mathrm{COP} = \frac{Q}{\dot{W}} \quad (2)$$

Here, the power consumption of the cooler is mainly from the air blowers to maintain the air flows.

2.2. Battery thermography

The development of battery thermal management requires an essential understanding of the complex battery thermal behavior which is deeply coupled with its electrochemical process during operation. In this work, we focus on large-format lithium-ion pouch cells of which the thermal performance is more critical than small cylindrical or prismatic cells. 20 Ah LFP cells from A123 Systems (see Fig. S1(a) of the Supplementary Information) were selected for investigation, and their dimensions are around 200 × 150 × 7 mm (L × W × δ). The cell density was measured by Archimedes law using a dielectric fluid (Thermal H10, Julabo). The cell bulk thermophysical properties, i.e., specific heat and anisotropic thermal conductivity, were characterized using a transient cooling method and a constant-temperature heating method, respectively [43]. A lock-in thermography experiment [44] was then set up to simultaneously measure the battery electrochemical and thermal responses during charging and discharging, as presented in Fig. 4 and Fig. S1(b). A pouch cell was placed in a custom-designed cell holder and connected to a high-power battery tester (BOP 10-100MG, KEPCO Inc.) where different current protocols can be applied at a maximum of 100 A. An infrared camera (A35sc, FLIR Systems) was employed to monitor the battery surface temperature during electrochemical tests.

The LFP pouch cell contains 42 unit cells (current collectors, cathode, separator, anode), which utilizes $LiFePO_4$ as the cathode and graphite as

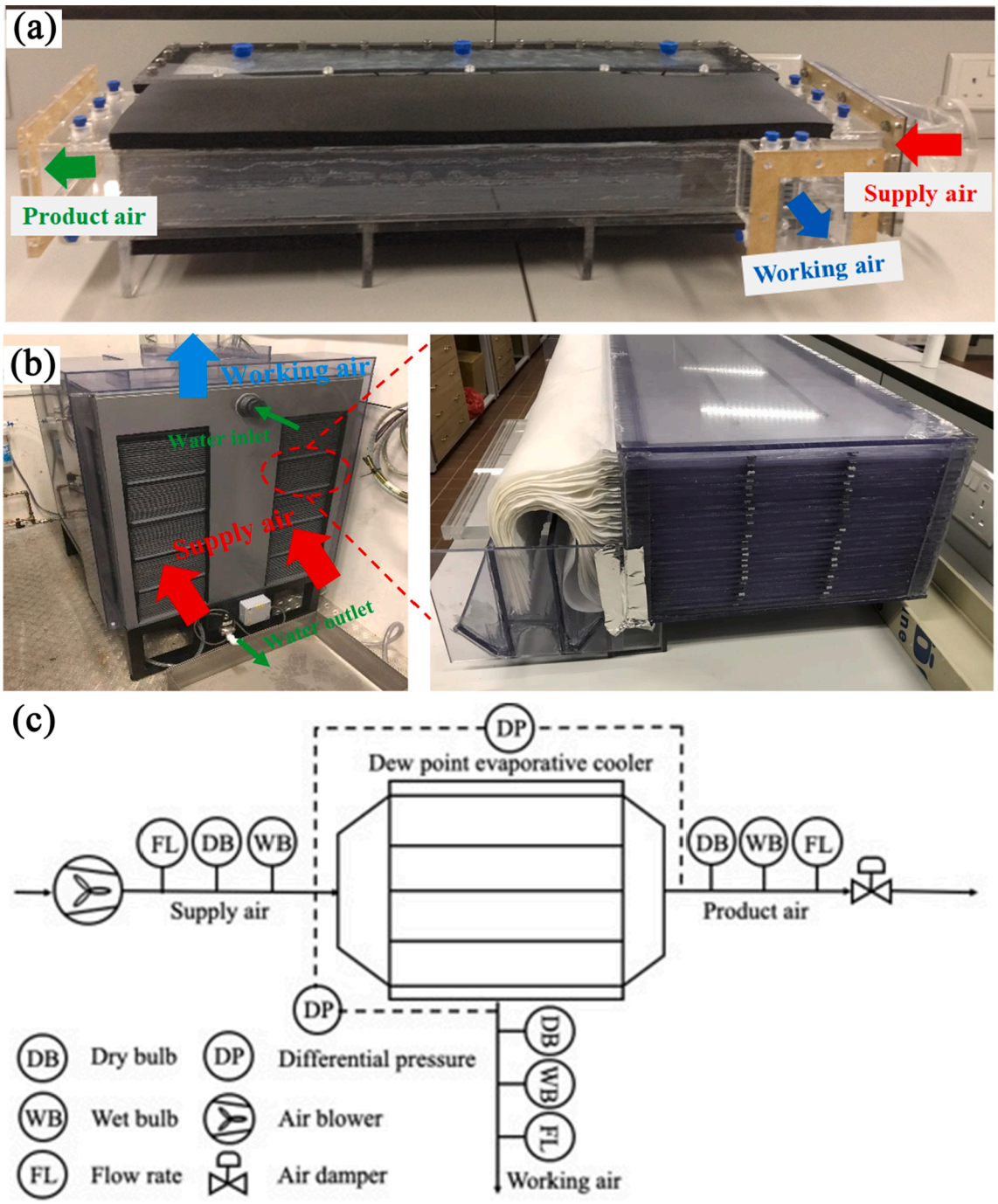

Fig. 3. Development of dew-point evaporative coolers. (a) A prototype-scale cooler. (b) A large cooler scaled up from the small cooler prototypes. The product air exits at the back of the cooler (not shown). (c) Test system of the coolers.

the anode. To obtain the physical dimensions of cell components, a cell was disassembled in a glovebox and three samples of each component were measured to take their average values, which are provided in Table S1 of the Supplementary Information. The half-cell reactions of the cathode and anode during charging/discharging are expressed as

$$Li_{y-x}FePO_4 + xLi^+ + xe^- \underset{\text{charge}}{\overset{\text{discharge}}{\leftrightarrows}} Li_yFePO_4 \quad (3)$$

$$Li_xC_6 \underset{\text{charge}}{\overset{\text{discharge}}{\leftrightarrows}} C_6 + xLi^+ + xe^- \quad (4)$$

The upper and lower voltage limits of the cell are 3.6 V and 2.5 V, which are denoted as 100 % and 0 % cell state of charge (SOC), respectively.

The battery electrochemical-thermal performance revealed from the thermography experiments was used to inform battery thermal management with dew-point evaporative cooling. The major research efforts carried out in this work are summarized in Fig. 4.

3. Modeling

3.1. Cooler model

A 2D computational fluid dynamics (CFD) model can be adopted to predict the cooling performance of the cooler at a steady state by considering the momentum, energy and mass balances in a generic

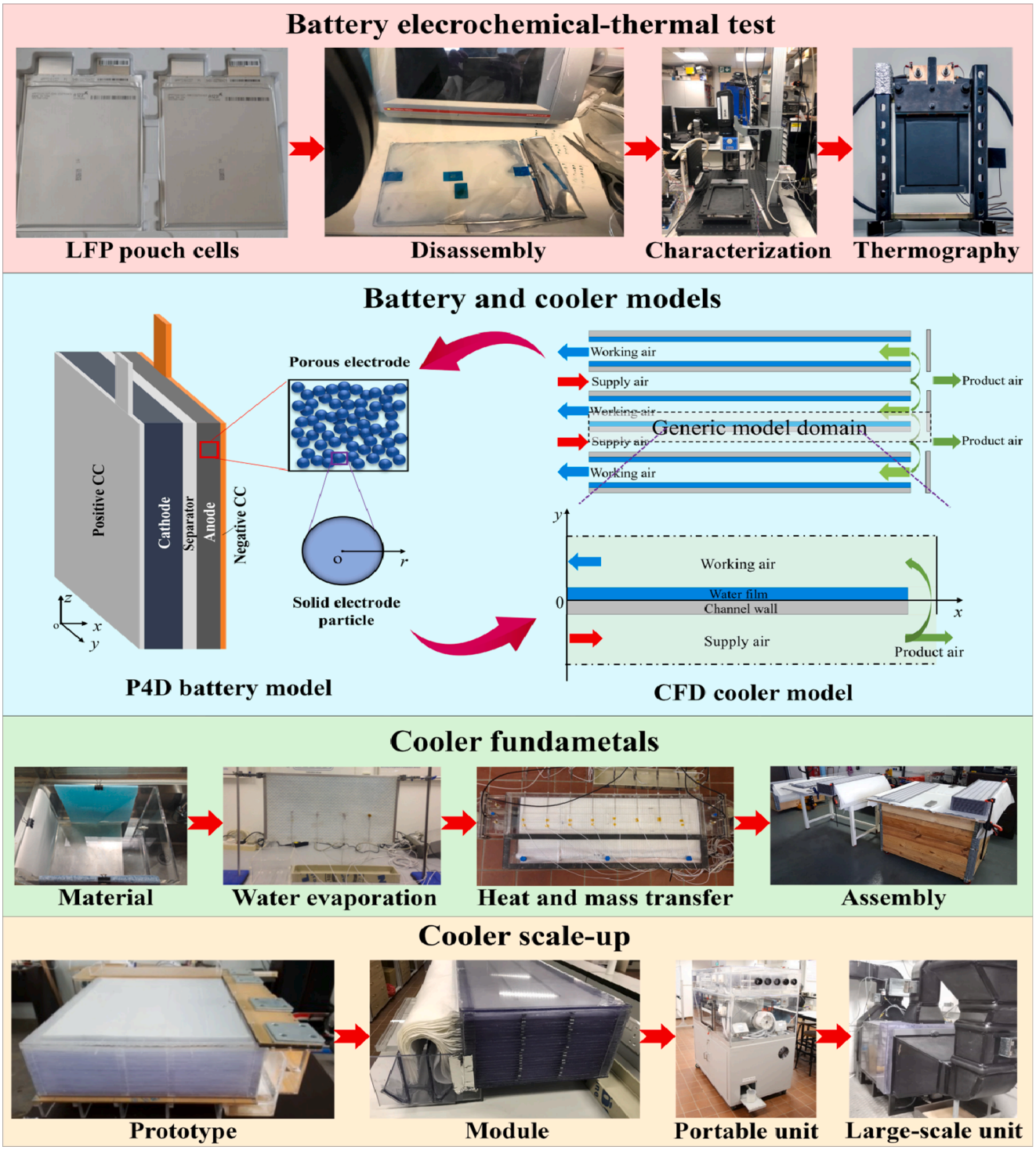

Fig. 4. Battery thermal management with scalable dew-point evaporative cooling.

channel geometry, as highlighted in Fig. 4. More information is also available in our previous work [45].

In the model, the air flows are assumed to be incompressible Newtonian fluid operating at laminar flow range (Re less than 2300), and the water film is stagnant and uniformly distributed on the wet channel surface. Hence, the governing equations for different domains of the cooler model geometry can be summarized as follows:

(1) Supply air flow.

$$\text{Momentum balance:} \rho_a(\vec{u}\cdot\nabla)\vec{u} = -\nabla P + \mu\nabla^2\vec{u} \quad (5)$$

$$\text{Continuity:} \nabla\cdot\vec{u} = 0 \quad (6)$$

$$\text{Energy balance}: \rho_a c_p \vec{u}\cdot\nabla T = k\nabla^2 T \quad (7)$$

(2) Working air flow.

$$\text{Momentum balance}: \rho_a(\vec{u}\cdot\nabla)\vec{u} = -\nabla P + \mu\nabla^2\vec{u} \quad (8)$$

$$\text{Continuity}: \nabla \cdot \vec{u} = 0 \tag{9}$$

$$\text{Energy balance}: \rho_a c_p \vec{u} \cdot \nabla T = k \nabla^2 T \tag{10}$$

$$\text{Species balance}: \vec{u} \cdot \nabla \rho_v = D_{va} \nabla^2 \rho_v \tag{11}$$

(3) Channel plate and water film.

$$\text{Energy balance}: k \nabla^2 T = 0 \tag{12}$$

where $\nabla = \left(\frac{\partial}{\partial x}, \frac{\partial}{\partial y}\right)$, $\vec{u} = (u_x, u_y)$.

3.2. Battery model

To capture the complex multiphysics mechanisms in batteries, a physics-based battery model is crucial and offers great help to predict phenomenological cell behaviors [46]. In general, developing a comprehensive battery model across multiple scales and dimensions is extraordinarily challenging. A simple but powerful battery model was developed by Doyle, Fuller and Newman (DFN) in a 'pseudo-2D' (P2D) geometry [5]. The model adopts the concentrated solution and porous electrode theories to account for diffusion, migration and convection of lithium ions in the electrolyte, as well as intercalation into solid particles. Following their work, several supplements or simplifications have been introduced to the P2D model to incorporate more physics or improve the computation efficiency [47]. However, the P2D model is not able to capture spatially non-uniform electrochemical reactions and transport phenomena, particularly on the transverse direction (perpendicular to the electrode thickness). Many existing studies thus do not account for heterogeneous processes (e.g., local heat generation) in the entire 3D geometry of a cell [48,49]. On the other hand, a direct extension of the DFN theory into a full 3D battery geometry would result in a computational-expensive framework, especially inefficient for practical cells with a multi-layer structure.

In this work, a new pseudo-4D (P4D) battery electrochemical-

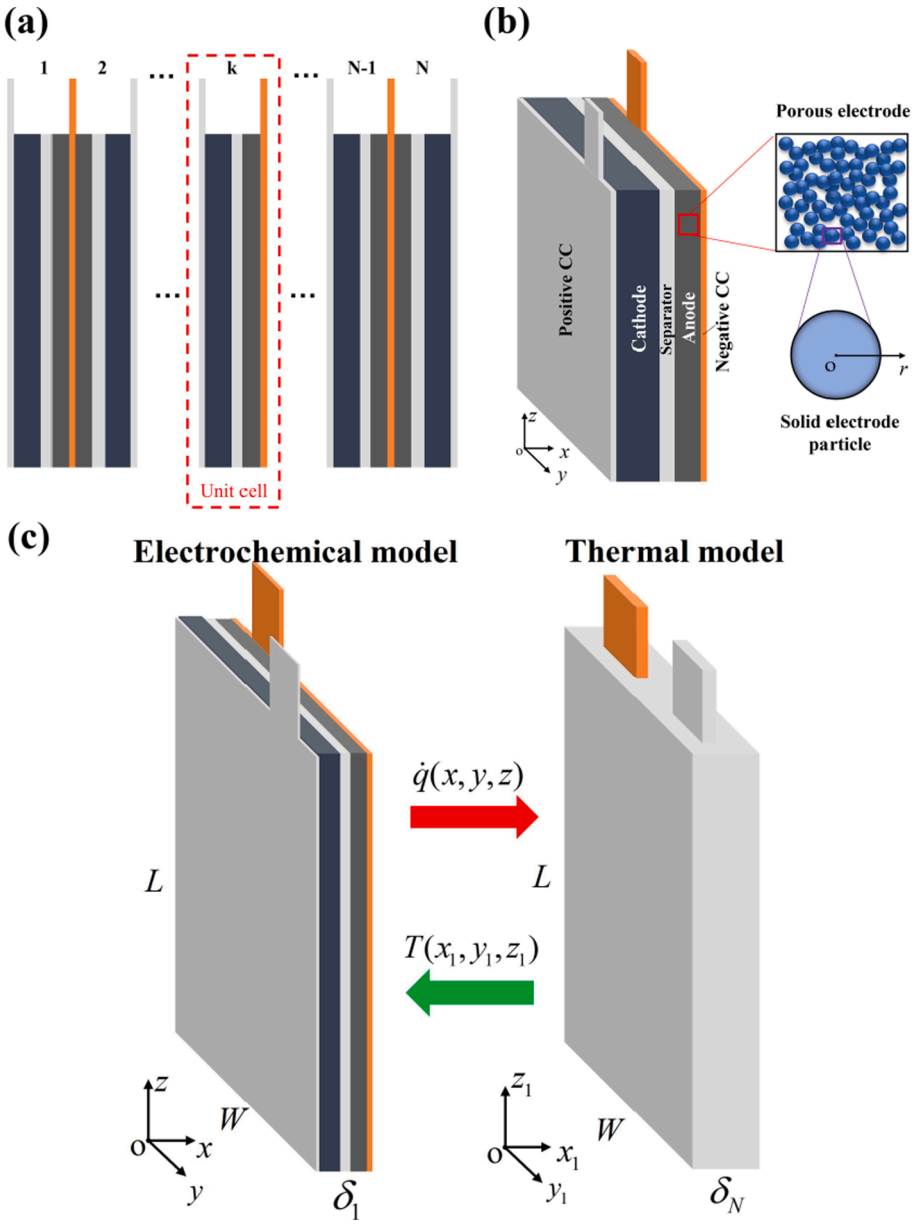

Fig. 5. Modelling of lithium-ion pouch cell. (a) Laminate structure of a pouch cell. (b) P4D electrochemical model geometry. (c) Full battery electrochemical-thermal model. δ_1 represents the thickness of a unit cell, and δ_N is the total thickness of N unit cells.

thermal model is proposed for large-format lithium-ion prismatic pouch cells that both achieves high computational efficiency and retains essential spatiotemporal physical information. Lithium-ion pouch cells usually have a laminate structure with layers of cathode, anode, separator, and positive and negative current collectors (CCs) to form multiple unit cells in parallel, as shown in Fig. 5(a). During charging and discharging, a similar electrochemical process will take place in different unit cells, hence a general battery model can be established to a single unit cell and extended to others. As illustrated in Fig. 5(b), a unit cell contains a pair of cathode, anode and separator, as well as half thickness of positive and negative CCs. The P4D battery electrochemical model is comprised of three spatial coordinates (x, y, z) for a full 3D cell geometry and an additional spatial coordinate (r) for the solid electrode particles which are assumed to be identical spheres. It considers charge and mass balances in both solid and liquid phases of a unit cell where local distributions of potential, current density, concentration and charge transfer rate are included. Lithium intercalation and diffusion in the solid electrode particles are taken into account in the radial direction. The electrochemical reaction rate is calculated via Butler-Volmer kinetics [50].

The battery model equations in different cell domains are written as follows:

(1) Electrodes (positive and negative).

$$\text{Charge balance in solid:} \nabla\cdot\overrightarrow{i_s} = -ai \tag{13}$$

$$\text{Charge balance in liquid :} \nabla\cdot\overrightarrow{i_l} = ai \tag{14}$$

$$\text{Mass balance in solid :} \frac{\partial c_s}{\partial t} = \frac{1}{r^2}\frac{\partial}{\partial r}\left(D_s r^2 \frac{\partial c_s}{\partial r}\right) \tag{15}$$

$$\text{Mass balance in liquid :} \varepsilon_l \frac{\partial c_l}{\partial t} + \nabla\cdot\overrightarrow{N_l} = \frac{ai}{F} \tag{16}$$

$$\text{Butler-Volmer kinetics:} i = i_0 c_l^{\alpha}\left(c_{s,\max} - c_{s,surf}\right)^{\alpha} c_{s,surf}^{1-\alpha}\left[\exp\left(\frac{\alpha F\eta}{RT}\right) - \exp\left(-\frac{(1-\alpha)F\eta}{RT}\right)\right] \tag{17}$$

where $\overrightarrow{i_s} = -\sigma^{eff}\nabla\phi_s$, $\overrightarrow{i_l} = -\kappa^{eff}\nabla\phi_l + \kappa_D^{eff}\nabla\ln c_l$, $\overrightarrow{N_l} = -D_l^{eff}\nabla c_l + \frac{\overrightarrow{i_l} t_+^0}{F}$, $\kappa_D^{eff} = \frac{2\kappa^{eff}RT}{F}\left(1 - t_+^0\right)$, $\eta = \phi_s - \phi_l - U_{eq}$.

(2) Separator

$$\text{Charge balance in liquid:} \nabla\cdot\overrightarrow{i_l} = 0 \tag{18}$$

$$\text{Mass balance in liquid :} \varepsilon_l \frac{\partial c_l}{\partial t} + \nabla\cdot\overrightarrow{N_l} = 0 \tag{19}$$

(3) Current collector (positive and negative).

$$\text{Charge balance in solid :} \nabla\cdot\overrightarrow{i_s} = 0 \tag{20}$$

In the battery model, the electrode OCP at different temperatures can be calculated from:

$$U_{eq}(T) = U_{eq,ref} + (T - T_{ref})\frac{dU_{eq}}{dT} \tag{21}$$

The charge transfer on the electrode–electrolyte surface is defined as:

$$-D_s\left.\frac{\partial c_s}{\partial r}\right|_{r=R_s} = \frac{i}{F} \tag{22}$$

The applied current (negative for discharge) is defined on the positive battery tab, while the negative battery tab is fixed at ground, written as:

$$\overrightarrow{n}\cdot\overrightarrow{i_s} = i_{app},\ \phi_s = 0 \tag{23}$$

The effective conducitivities and diffusivities are calculated via Bruggeman correlation [50], expressed as follows:

$$\sigma^{eff} = \varepsilon_s^{brug}\sigma,\ \kappa^{eff} = \varepsilon_l^{brug}\kappa,\ D_l^{eff} = \varepsilon_l^{brug}D_l \tag{24}$$

In addition, a symmetric boundary is applied on the external surfaces of positive and negative CCs to indicate the iterative geometry of unit cells.

Heat generation is associated with electrochemical reactions during battery operation, including joule heat, reaction heat and entropic heat which can be formulated as [50,51]:

$$\dot{q}_j = \sigma^{eff}\nabla\phi_s\cdot\nabla\phi_s + \kappa^{eff}\nabla\phi_l\cdot\nabla\phi_l + \kappa_D^{eff}\nabla\ln c_l\cdot\nabla\phi_l \tag{25}$$

$$\dot{q}_r = ai\eta \tag{26}$$

$$\dot{q}_e = aiT\Delta S \tag{27}$$

To investigate the thermal effect of the electrochemical process, a battery thermal model is necessary. As battery external surfaces are usually subjected to certain thermal boundary conditions, such as convection and conduction, the entire battery geometry should be considered in the thermal model to accurately capture its temperature distribution. However, modeling the electrochemical process of all the unit cells together with heat transfer is computationally expensive and time-consuming. Therefore, a cross-scale coupling of the electrochemical model and thermal model is proposed. As shown in Fig. 5(c), the spatially varying heat generation in the P4D battery electrochemical model is linearly projected into the 3D battery thermal model, where the heat generation rate through cell thickness is proportionally expanded from the unit cell to the bulk cell. The bulk cell in the thermal model is deemed homogeneous which neglects the laminate structure of a real battery but has the effective thermophysical properties from the contributions of different components. This simplification allows the battery thermal model to retain the spatial resolution of battery intrinsic thermal process without introducing a considerable amount of model complexity. Inversely, the obtained temperature field from the battery thermal model is redirected into the electrochemical model of a unit cell via a similar projection. The temperature gradient imposed on the unit cell will further impact its physicochemical properties and the heterogeneity in lithium concentration, current density, and charge transfer, etc.

A general energy balance equation can be formulated for the battery thermal model as [51]:

$$\rho c_p\frac{\partial T}{\partial t} = \nabla\cdot(k\nabla T) + \dot{q} \tag{28}$$

where the total heat generation is a sum of joule heat, reaction heat and entropic heat in the electrodes, while only joule heat exists in the current collectors and separator. The effective thermophysical properties (density, specific heat and thermal conductivity) of the bulk cell are available in Table S1 of the Supplementary Information.

Convective heat transfer is assumed to take place on all battery external surfaces, expressed as:

$$\overrightarrow{n}\cdot(-k\nabla T) = h(T - T_{amb}) \tag{29}$$

To estimate the cooling potential of a dew-point evaporative cooler for battery thermal management, it is assumed that a battery is immersed in the cooling air delivered by the cooler, where the air flow is large enough to stay at a constant temperature. The coupled electrochemical-thermal performance of the battery upon cooling can be simulated and compared to a reference case where the cooler is absent.

The models of dew-point evaporative cooler and lithium-ion battery

are established in COMSOL Multiphysics platform and numerically solved using the finite element method. As shown in Fig. 6, relevant parameters are input to each model and the product air temperature from the cooler model is extracted and imported into the battery model as the ambient condition for heat convection. The battery electrochemical-thermal model is finally solved for its voltage and temperature responses.

4. Results and discussion

4.1. Dew-point evaporative cooler performance

The performance of the prototype-scale and large-scale coolers were judiciously investigated under different supply air temperature, humidity, velocity and working air ratio. Fig. 7 shows the product air temperature and COP of the coolers, and their detailed test conditions are available in Table S1 and S2 of the Supplementary Information. The supply air humidity to the prototype-scale cooler was maintained at around 11.0 g/kg while other parameters (temperature, velocity and working air ratio) were individually adjusted. The large-scale cooler was tested at two humidity conditions (ambient and dehumidified), which were controlled via an in-line dehumidifier installed before the cooler [52]. When the supply air velocity and working air ratio were adjusted, dehumidified air was used for testing the large-scale cooler.

It was first observed from Fig. 7(a) that the prototype-scale cooler could deliver the product air temperature between 15.9 and 23.3 °C, and the COP was above 8.5 and could be as high as 27.4. This exhibits promising cooling potential for battery thermal management, at little additional cost of electricity in compared to forced convection. More importantly, as the cooler prototype was scaled up to a practical size with 2.9–6.7 kW cooling capacity (see Table S2), it still presented consistently excellent cooling effectiveness at 18.9–25.9 °C product air temperature and energy efficiency at 8.9–28.9 COP, as depicted in Fig. 7 (b). At high humidity, the product air temperature only rose by less than 5.0 °C which was still sufficient to cool batteries. Therefore, the ease of upsizing with enormous capacity and great stability to process the ambient air makes dew-point evaporative cooling extremely favorable for thermal management of large battery energy storage systems.

Subsequently, the cooler model is validated with the experimental product air temperature, working air temperature and COP of the two coolers in Fig. S4 of the Supplementary Information. As can be seen, the model achieves a good agreement with the experiment, and the maximum discrepancy is within ± 7.0 %. The root-mean-square errors (RMSEs) of the simulations are 0.4 °C for product air temperature, 0.7 °C for working air temperature and 0.6 for COP.

4.2. Battery electrical and thermal behaviors

Lock-in thermography experiments were carried out on the LFP pouch cells using square-wave alternating current between charge and discharge at 4C-rate (80 A) and 100 s cycle time, as illustrated in Fig. 8 (a). The original datasets of all lock-in thermography experiments are provided in Oxford University Research Archive (ORA) [53]. Accordingly, the cell SOC and voltage varied at an average value. The initial SOCs of the cells were adjusted so that the average cell SOCs in the tests averaged out at 30 %, 50 % and 70 %, respectively. The initial cell SOC was obtained by discharging the cells from 100 % SOC via Coulomb counting. The cell voltage and surface temperature distributions in these tests can be used to simultaneously parameterize several important battery physicochemical properties [54], and they are used to validate the proposed battery model in this work. A detailed list of the model parameters is provided in Table S3 and S4 of the Support Information, and the open circuit potential (OCP, U_{eq}) and temperature gradient of OCP (dU_{eq}/dT) for LFP and graphite electrodes are shown in Fig. S2 of the Supplementary Information.

Fig. 8 shows the test and simulation results of a lock-in thermography experiment at 50 % cell SOC. Three temperatures, i.e., the hot spot temperature, cold spot temperature and average surface temperature are selected to plot in Fig. 8(a). As shown in Fig. 8(b), the cell surface temperature was observed to be non-uniform. A hot spot (highlighted in red square) appeared and remained stable at the top center of the cell during the square-wave cycling. The bottom corners of the cell were found to be relatively cool, and a cold spot (highlighted in blue square) was defined at the left bottom corner. In this test, while the cell

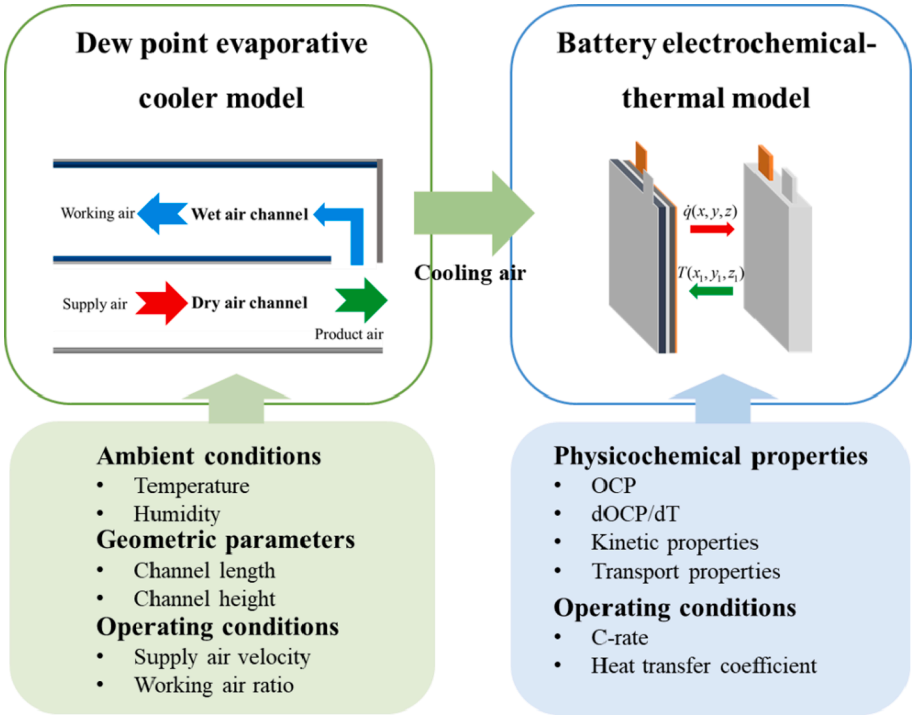

Fig. 6. Multiphysics coupling of dew-point evaporative cooler model and P4D electrochemical-thermal battery model.

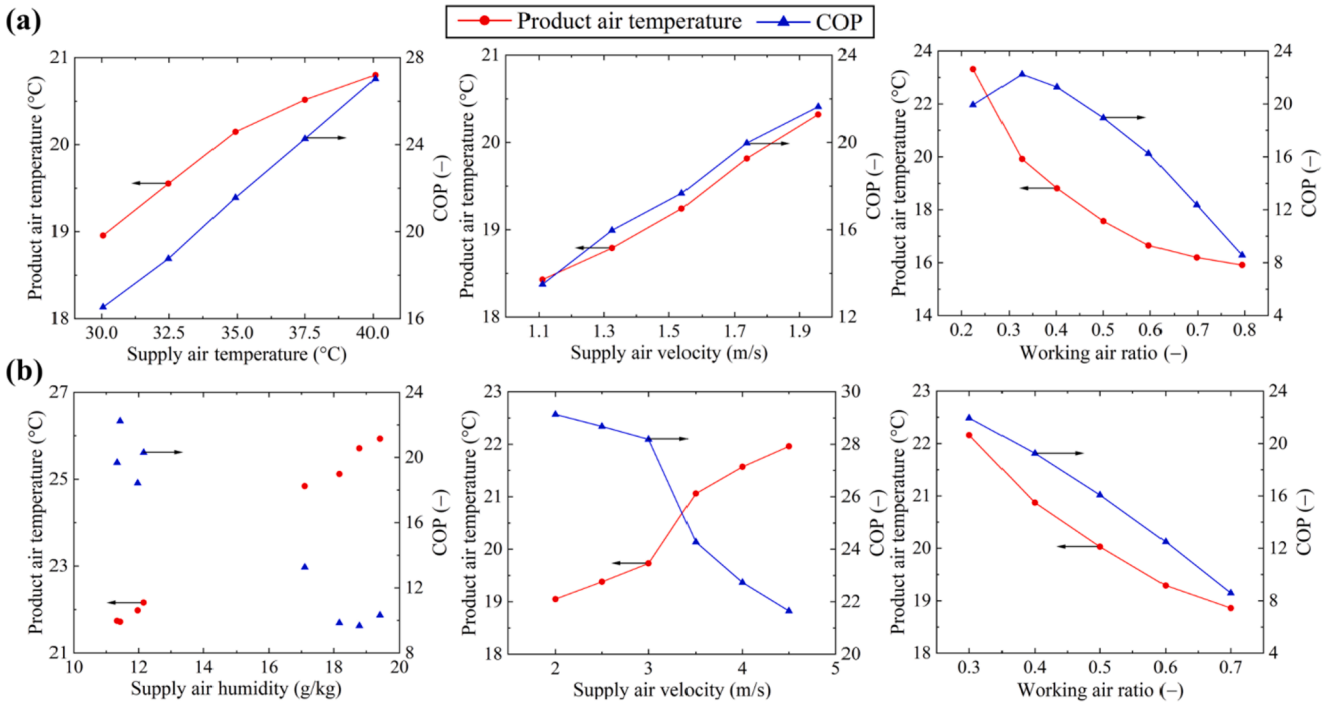

Fig. 7. Test results of product air temperature and COP under varying supply air temperature, humidity, velocity and working air ratio for: (a) Prototype-scale cooler. (b) Large-scale cooler. Two humidity conditions (ambient and dehumidified) were tested in the large cooler.

temperature was rising due to a positive heat generation from joule heating and electrochemical reactions, local temperature fluctuations were observed as the applied current switched between charging and discharging. This is ascribed to the entropic heating of which the sign (positive or negative) was reversed as the applied current alternated. The dynamic electrical and thermal behaviors of the cell can be well captured in the simulations by the pseudo-4D battery model, as shown in Fig. 8(c). The formation and expansion of the hot spot are clearly predicted at identical time steps. The surface temperature gradient can be accurately reproduced in the simulation, although minor discrepancy exists in some small local areas. The RMSEs for the cell voltage and temperature are found to be 32 mV and 0.3 °C, respectively. In addition, the cell test and simulation results at 30 % and 70 % SOC are provided in Fig. S3, and similar phenomena to those at 50 % SOC were observed.

4.3. Battery thermal management with dew-point evaporative cooling

Battery electrochemical-thermal performance under full charge/discharge cycles with dew-point evaporative cooling for thermal management can be investigated via the coupling of cooler and battery models. In our simulation, the battery cell was set to discharge at 4C from 100 % SOC which corresponds to the applied current used in the lock-in thermography. All cell surfaces were subjected to convective heat transfer with $h = 15$ W/(m^2·K), which was similar to the value obtained from battery thermal characterization experiments [43,54]. The large-scale cooler was employed for the model coupling and its cooling effect on the battery is compared to a reference case without air pre-cooling. The cooler was assumed to operate at 4.5 m/s supply air velocity and 0.33 working air ratio, which is the nominal condition in Table S2 and S3. Ambient air was supplied to the cooler and the consequent product air was delivered to interact with the battery. In contrast, the battery performance without evaporative cooling was examined under identical conditions, while ambient air was circulated to dissipate heat from the battery.

Fig. 9(a) illustrates the voltage, average temperature rise and temperature variation ($T_{max} - T_{min}$) of a LFP pouch cell during a full-discharge process. The cell voltage discharging at 30.0 °C constant cell temperature is also plotted as a reference. With dew-point evaporative cooling, the air temperature was reduced to 19.5 °C ($\Delta T = 10.5$ °C) prior to cooling the battery. Consequently, the average cell temperature remained almost stable before 50 % depth of discharge (DoD). Owing to a large voltage drop and concomitant heat generation towards the end of discharge, the battery temperature gradually increased to 37.6 °C. Nonetheless, the battery temperature was controlled at 32.0 °C in average throughout the full discharge. In contrast, the battery without pre-cooling the ambient air for heat dissipation had a continuous temperature rise to above 45.0 °C during discharge. Although temperature rise could be harmful to battery safety and durability, it had a positive effect on cell voltage platform and reversible capacity, as shown in Fig. 9 (a). The battery without evaporative cooling had a higher voltage output with 19.0 % (3.1 Ah) larger available cell capacity than that at constant-temperature discharge, and 6.3 % (1.2 Ah) higher capacity than the cell with evaporative cooling. This is attributed to higher cell open-circuit voltage, exchange current density and lithium diffusivity at elevated temperature [55]. Nonetheless, considering the accelerated aging mechanisms (e.g., solid electrolyte interphase (SEI) layer growth and electrolyte decomposition [56]) which often occur at higher battery temperature and ultimately lead to increased internal resistance and capacity fade, it is preferrable to operate batteries at controlled temperatures.

Furthermore, active cooling could alter the temperature distribution within the cell, as can be seen in Fig. 9(b)-(c). Owing to greater heat convection rate, the cell upon evaporative cooling exhibited lower temperature levels with improved temperature uniformity at cell center, though slightly larger temperature gradient may be seen near the corners where less active material is available. Whereas in a non-evaporative cooling environment, cell-surface heat flux to the ambient was much more slowly so more heat can accumulate in the cell, leading to a serious hot spot confined in a small region on cell surface. Therefore, it is important to note that battery cooling can possibly improve temperature uniformity, while reducing the bulk cell temperature. In both cases, the cell temperature variation exhibited a plateau at *c.a.* 60–80 % DoD and was followed by a sharp increase. This phenomenon is mainly attributed to the substantial cell temperature rise from joule and

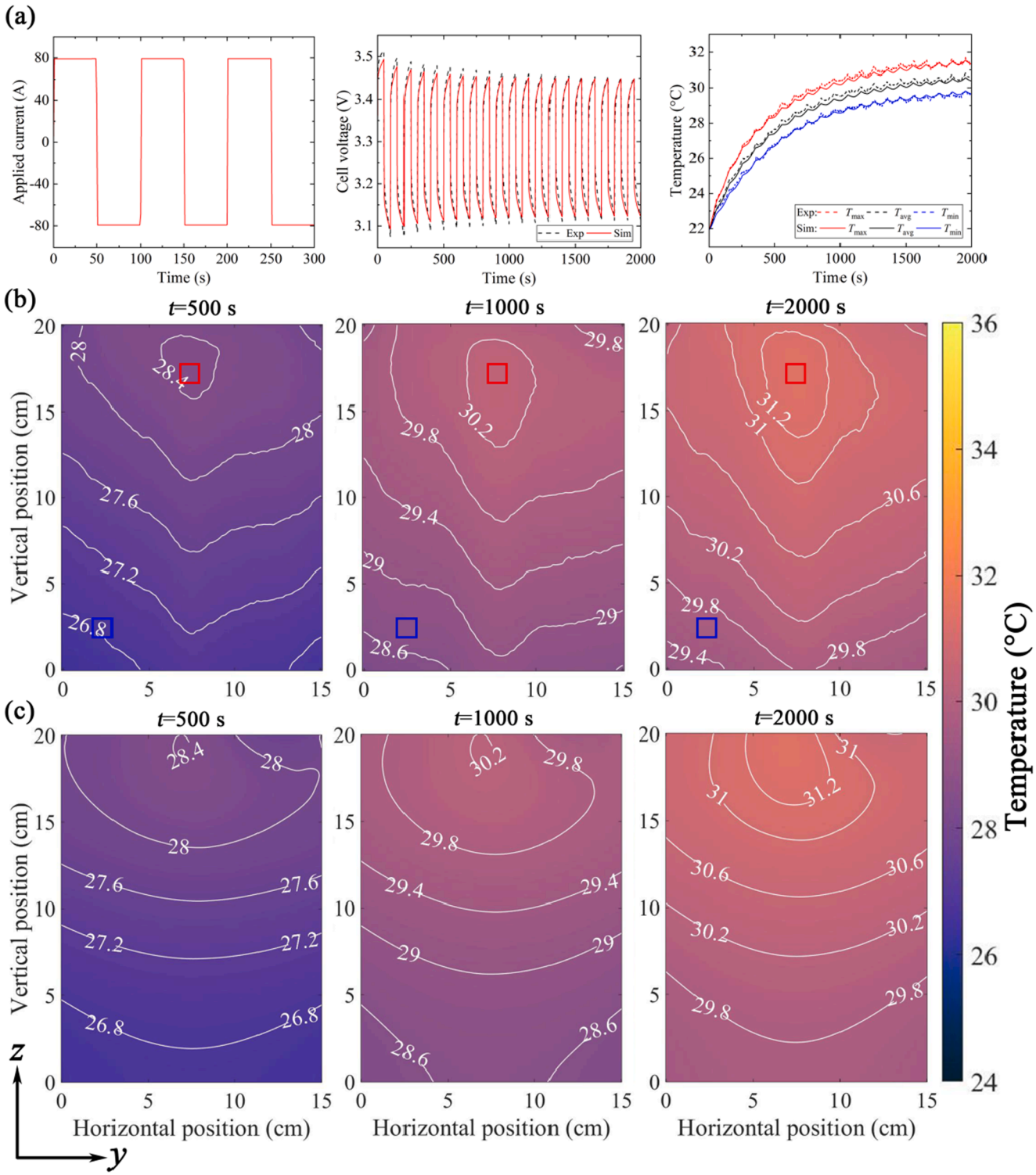

Fig. 8. Battery thermography test and simulation results under square-wave cycling with 4 C-rate and 100 s cycle time applied current at 50 % SOC. (a) Applied current, cell voltage and three temperatures at hot spot (T_{max}), cold spot (T_{min}) and surface average (T_{avg}). The experimental data and simulation results are plotted in solid and dash lines, respectively. (b) Cell surface temperature distribution at $t = 500$ s, 1000 s and 2000 s. The locations of the hot spot (red) and cold spot (blue) are marked in square. (c) Simulation of (b) with the proposed P4D model. The battery tabs (not shown) locate at the top edge of cell thermal images in (b) and (c).

reversible heating after 80 % DoD, which imposes a significant temperature drop from the cell center to edges. The reversible heating arises from the entropy changes of LFP and graphite electrodes. As shown in Fig. S2 of the Supplementary Information, the LFP electrode (lithiation during discharge) shows large negative entropy change after 90 % SOC, while the graphite electrode (delithiation during discharge) presents positive values with similar magnitude at below 15 % SOC. Both electrodes will release a considerable amount of heat at the end of discharge and aggravate the temperature variation.

It is also noteworthy that the location of temperature hot spot in the cell was not fixed during full discharge/charge process. It initially formed at the top edge of the cell which was connected to the battery

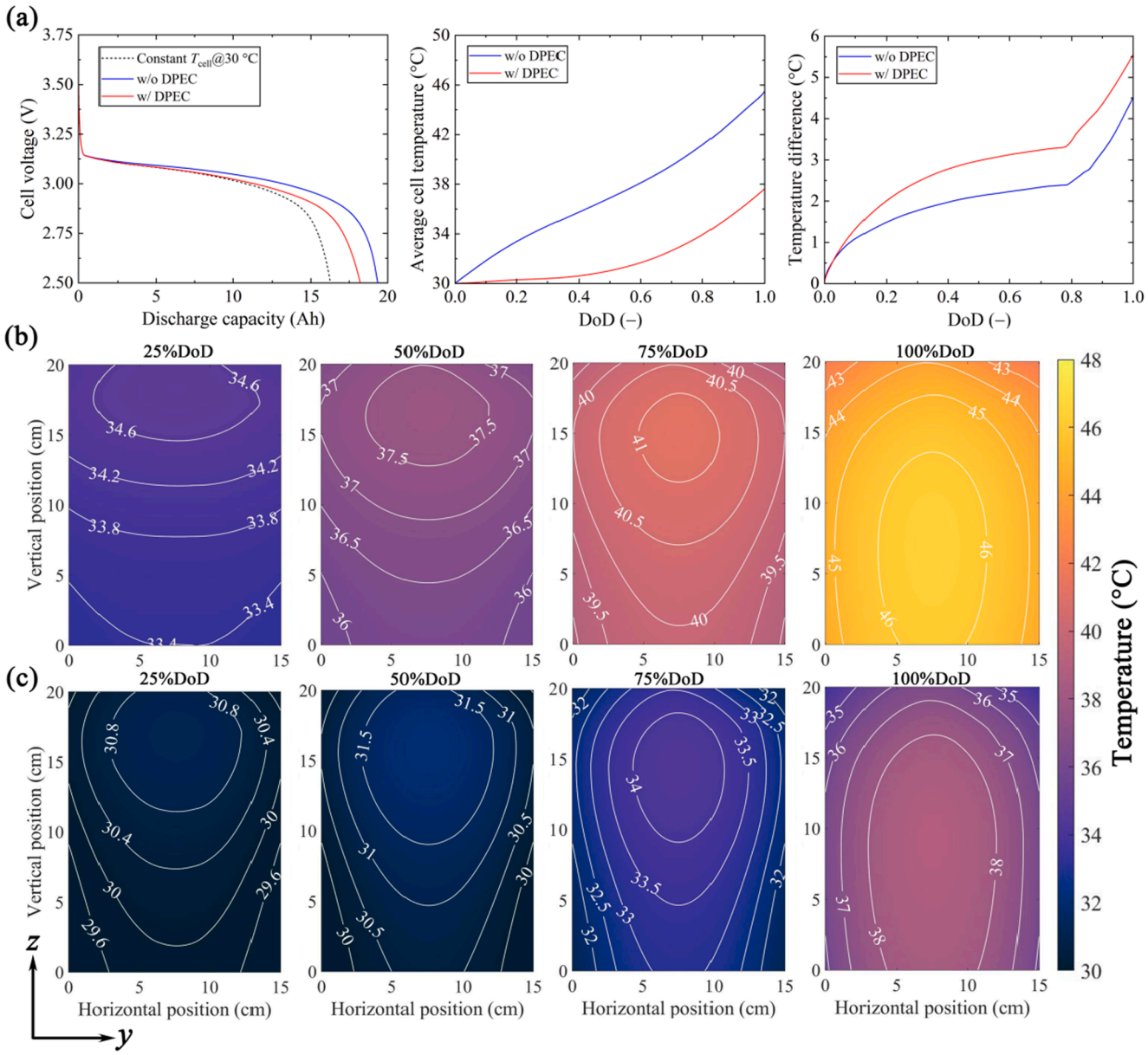

Fig. 9. Simulation of battery electrochemical-thermal performance under 4C full discharge from 100 % SOC with dew-point evaporative cooling for thermal management. The cases with only forced air convection (without DPEC) and 30 °C constant cell temperature are provided for comparison. (a) Cell voltage, average temperature and temperature variation. (b) Surface temperature distribution without DPEC at 25 %, 50 %, 75 % and 100 % DoD. (c) Surface temperature distribution with DPEC at 25 %, 50 %, 75 % and 100 % DoD. The battery tabs (not shown) locate at the top edge of cell thermal images in (b) and (c).

tabs and moved downwards to the bottom at the end of discharge. The hot spot was a good sign of current heterogeneity and indicated where the majority electrochemical reaction took place [57]. Hence, for large-format batteries, the dynamic thermal behavior is crucial to their rate capability, lifetime and safety, and should be carefully examined.

4.4. *Effect of working conditions on thermal management*

The battery thermal performance can be affected by its working conditions (air cooling, C-rate and convective heat transfer). In particular, the effectiveness of air cooling brought by a dew-point evaporative cooler (see Fig. 7) is greatly influenced by the ambient (temperature, humidity) and its operating conditions (supply air velocity, working air ratio). We further explored the battery electrochemical and thermal performance under different working conditions by conducting full discharge simulations. Detailed simulation conditions of the battery and cooler are listed in Table S5 of the Supplementary Information. When one parameter was varied, the others remained at their nominal values, and the initial cell temperature was assumed to equilibrate with the ambient temperature.

The effect of dew-point evaporative cooling on cell voltage and temperature responses under each working condition was observed to be consistent with those in Fig. 9. Hence, we specifically compared the average cell temperature at the end of discharge (EoD) under cooling (with DPEC) and non-cooling (without DPEC) cases, as an attempt to reveal the feasibility of dew-point evaporative cooling. the air cooling achieved by the cooler is provided in Fig. 10, and the simulation results are plotted in Fig. 11. As can be seen in Fig. 10, the dew-point evaporative cooler could reduce the ambient air temperature by more than 10 °C for most cases, with a maximum at 18.1 °C. Only when the ambient temperature itself is low enough ($T_{amb} = 20$ °C) or the ambient humidity is limited with evaporative cooling potential ($\omega_{amb} = 18$ g/kg), the temperature reduction brought by the cooler did not look immediately appealing.

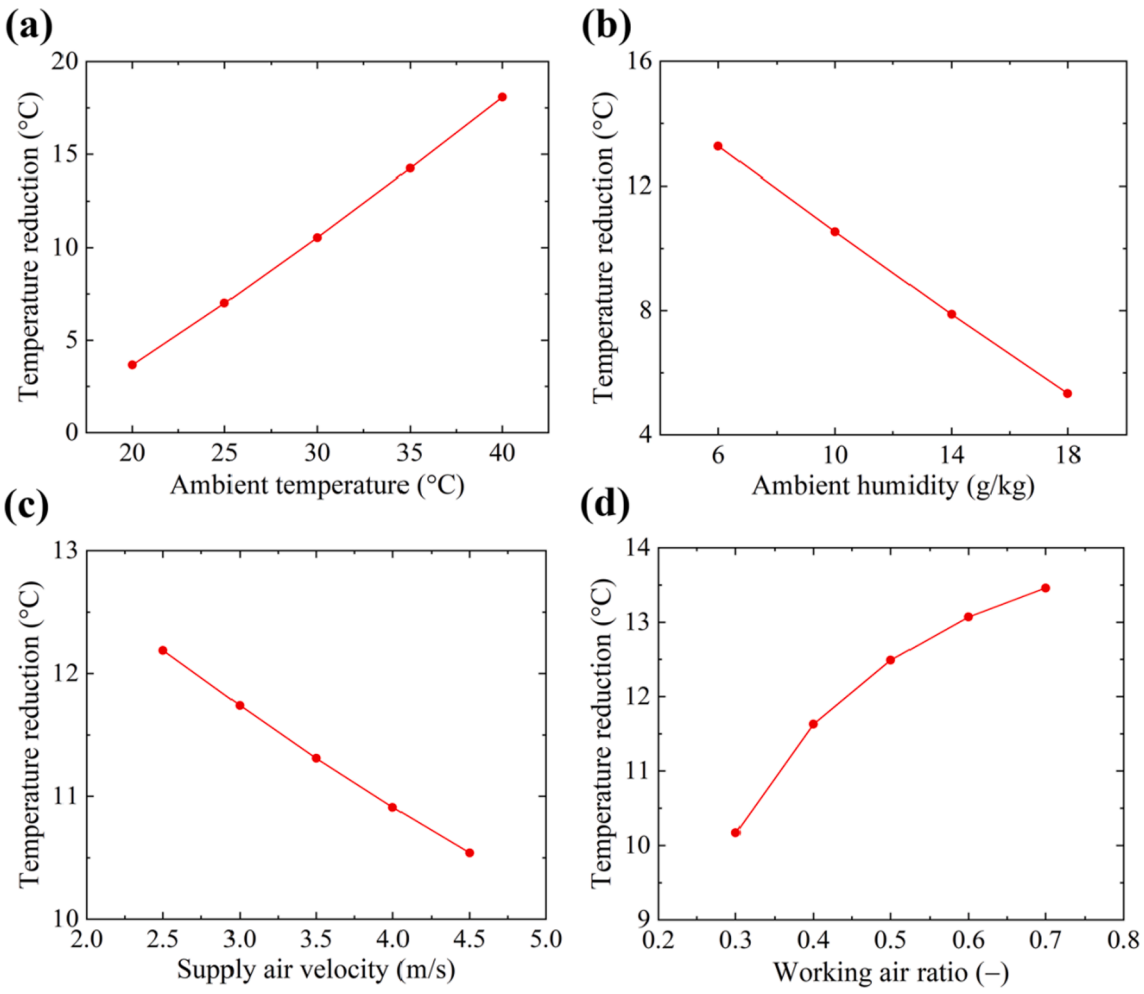

Fig. 10. Temperature reduction ($T_{amb} - T_p$) achieved by the dew-point evaporative cooler under different (a) ambient temperature, (b) ambient humidity, (c) supply air velocity and (d) working air ratio.

For a battery discharging at 4C and $h = 15$ W/(m^2·K), as shown in Fig. 11(a)-(d), the average cell temperature rose by around 15.0 °C at EoD, if without evaporative cooling. In contrast, dew-point evaporative cooling dramatically limited the cell temperature to below or around 40.0 °C, which was 3.0–13.6 °C lower than the non-cooling case. Additionally, the cell temperature rise was proportional to the battery discharge C-rate (see Fig. 11(e)), and the effect of evaporative cooling was more pronounced at lower C-rates, when the cell could be cooled below its initial temperature. Enhancing the convective heat transfer coefficient from 5 to 25 W/(m^2·K) also effectively reduced the average cell temperature at EoD (see Fig. 11(f)), which led to more significant temperature difference (4.1–9.4 °C) between the cooling and non-cooling cases.

5. Conclusions

Owing to its high energy efficiency and great sensible cooling effectiveness, dew-point evaporative cooling is proposed as a novel approach for battery thermal management. A scalable dew-point evaporative cooling technology was developed, and a practical-scale cooler device was fabricated which exhibited consistent cooling feasibility as the lab-scale prototypes. The large-scale cooler presented 2.9–6.7 kW cooling capacity and 8.9–28.9 COP, while it could deliver the product air temperature at 18.9–25.9 °C after cooling the ambient air. Concurrently, the complex dynamic cell electrical and thermal responses of a large-format 20 Ah LFP pouch cell was investigated as a case study for thermal management. The cell temperature development was well captured via lock-in thermography experiments and accurately accounted for by a newly developed P4D electrochemical-thermal model.

The potential of the dew-point evaporative cooling for battery thermal management could be revealed via a multi-physics coupling of the cooler and battery models. This work elucidated that dew-point evaporative cooling could effectively dissipate heat from a battery so that it maintained an ideal operating temperature range within 20–40 °C. Compared to the cases with only ambient air convection, dew-point evaporative cooling could pre-cool the ambient air by up to 18.1 °C and control cell average temperature to be 3.0–13.6 °C lower. In addition, dew-point evaporative cooling could alter cell temperature distribution during full discharge/charge cycles. Temperature uniformity at cell center was improved with less significant temperature rise and heat accumulated at the hot spot.

CRediT authorship contribution statement

Jie Lin: Conceptualization, Methodology, Investigation, Resources, Writing – original draft, Writing – review & editing. **Howie N. Chu:** Methodology, Investigation, Resources, Writing – review & editing. **Kyaw Thu:** Methodology, Writing – review & editing. **Malgorzata Wojtala:** Resources, Writing – review & editing. **Fei Gao:** Conceptualization, Methodology, Writing – review & editing. **Kian Jon Chua:** Supervision, Project administration, Funding acquisition, Writing – review

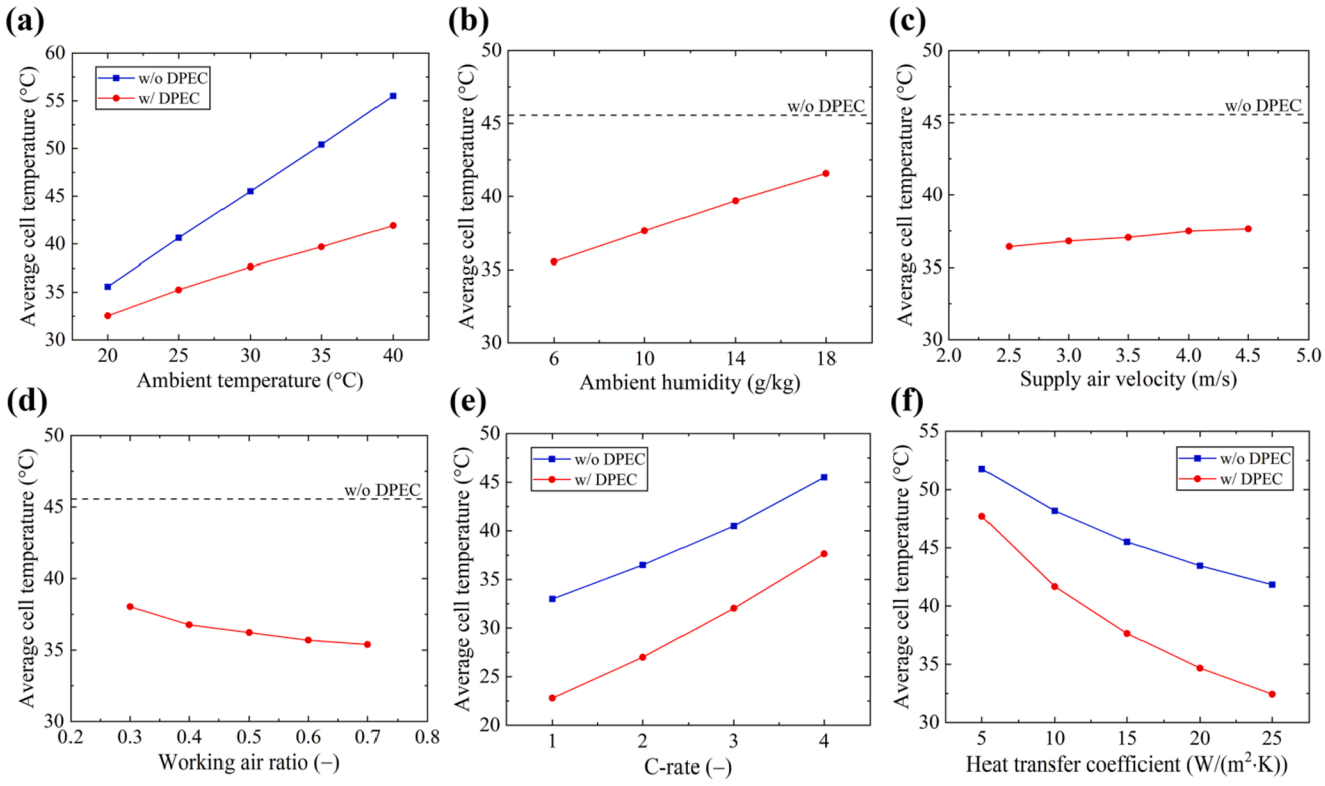

Fig. 11. Simulation of average cell temperature at EoD of full discharge under different battery and cooler working conditions. (a) Ambient temperature. (b) Ambient humidity. (c) Supply air velocity. (d) Working air ratio. (e) C-rate. (f) Heat transfer coefficient.

& editing.

Declaration of Competing Interest

The authors declare that they have no known competing financial interests or personal relationships that could have appeared to influence the work reported in this paper.

Data availability

Data will be made available on request.

Acknowledgements

The authors gratefully acknowledge the funding from (1) the UK Engineering and Physical Sciences Research Council (EPSRC) Translational Energy Storage Diagnostics (TRENDs) project; (2) the STFC Futures Early Career Award; (3) the Faraday Institution Multiscale Modelling project (Faraday.ac.uk; EP/S003053/1, grant number FIRG003); and (4) the National Research Foundation (NRF) Singapore under the Energy Innovation Research Programme (EIRP) Funding Scheme (R-265-00-543-279).

Appendix A. Supplementary material

Supplementary data to this article can be found online at https://doi.org/10.1016/j.enconman.2023.116948.

References

[1] Dietz T, Shwom RL, Whitley CT. Climate Change and Society. Annu Rev Sociol 2020;46:135–58.
[2] Chu S, Cui Y, Liu N. The path towards sustainable energy. Nat Mater 2016;16:16–22.
[3] Dunn B, Kamath H, Tarascon J-M. Electrical energy storage for the grid: a battery of choices. Science 2011;334:928–35.
[4] Gibb BC. The rise and rise of lithium. Nat Chem 2021;13:107–9.
[5] Newman J, Thomas-Alyea KE. Electrochemical systems. John Wiley & Sons; 2012.
[6] Robinson J, Shearing P, Brett D. Thermal Imaging of Electrochemical Power Systems: A Review. Journal of Imaging 2016;2:2.
[7] Ma S, Jiang M, Tao P, Song C, Wu J, Wang J, et al. Temperature effect and thermal impact in lithium-ion batteries: A review. Prog Nat Sci: Mater Int 2018;28:653–66.
[8] Feng X, Ouyang M, Liu X, Lu L, Xia Y, He X. Thermal runaway mechanism of lithium ion battery for electric vehicles: A review. Energy Storage Mater 2018;10:246–67.
[9] Liu H, Wei Z, He W, Zhao J. Thermal issues about Li-ion batteries and recent progress in battery thermal management systems: A review. Energ Convers Manage 2017;150:304–30.
[10] Wang Q, Jiang B, Li B, Yan Y. A critical review of thermal management models and solutions of lithium-ion batteries for the development of pure electric vehicles. Renew Sustain Energy Rev 2016;64:106–28.
[11] Wang Y, Gao Q, Wang G, Lu P, Zhao M, Bao W. A review on research status and key technologies of battery thermal management and its enhanced safety. Int J Energ Res 2018;42:4008–33.
[12] Wang T, Tseng KJ, Zhao J, Wei Z. Thermal investigation of lithium-ion battery module with different cell arrangement structures and forced air-cooling strategies. Appl Energ 2014;134:229–38.
[13] Wu W, Wang S, Wu W, Chen K, Hong S, Lai Y. A critical review of battery thermal performance and liquid based battery thermal management. Energ Convers Manage 2019;182:262–81.
[14] An Z, Jia L, Li X, Ding Y. Experimental investigation on lithium-ion battery thermal management based on flow boiling in mini-channel. Appl Therm Eng 2017;117:534–43.
[15] Wei T, Xiaoming X, Hua D, Yaohua G, Jicheng L, Hongchao W. Sensitivity Analysis of the Battery Thermal Management System with a Reciprocating Cooling Strategy Combined with a Flat Heat Pipe. ACS Omega 2020;5:8258–67.
[16] Malik M, Dincer I, Rosen MA. Review on use of phase change materials in battery thermal management for electric and hybrid electric vehicles. Int J Energ Res 2016;40:1011–31.
[17] Wu S, Li T, Tong Z, Chao J, Zhai T, Xu J, et al. High-Performance Thermally Conductive Phase Change Composites by Large-Size Oriented Graphite Sheets for Scalable Thermal Energy Harvesting. Adv Mater 2019;31:e1905099.
[18] Wang Z, Zhang Z, Jia L, Yang L. Paraffin and paraffin/aluminum foam composite phase change material heat storage experimental study based on thermal management of Li-ion battery. Appl Therm Eng 2015;78:428–36.
[19] Wu W, Yang X, Zhang G, Ke X, Wang Z, Situ W, et al. An experimental study of thermal management system using copper mesh-enhanced composite phase change materials for power battery pack. Energy 2016;113:909–16.

[20] Lin C, Xu S, Chang G, Liu J. Experiment and simulation of a LiFePO4 battery pack with a passive thermal management system using composite phase change material and graphite sheets. J Power Sources 2015;275:742–9.
[21] Xu J, Chao J, Li T, Yan T, Wu S, Wu M, et al. Near-Zero-Energy Smart Battery Thermal Management Enabled by Sorption Energy Harvesting from Air. ACS Central Science; 2020.
[22] Yang Y, Cui G, Lan CQ. Developments in evaporative cooling and enhanced evaporative cooling - A review. Renew Sustain Energy Rev 2019;113.
[23] Pandelidis D, Cichoń A, Pacak A, Drąg P, Drąg M, Worek W, et al. Performance study of the cross-flow Maisotsenko cycle in humid climate conditions. Int Commun Heat Mass 2020;115.
[24] Kashyap S, Sarkar J, Kumar A. Comparative performance analysis of different novel regenerative evaporative cooling device topologies. Appl Therm Eng 2020;176.
[25] Shahzad MW, Burhan M, Ybyraiymkul D, Oh SJ, Ng KC. An improved indirect evaporative cooler experimental investigation. Appl Energ 2019;256.
[26] Lin J, Thu K, Karthik S, Shahzad MW, Wang R, Chua KJ. Understanding the transient behavior of the dew point evaporative cooler from the first and second law of thermodynamics. Energ Convers Manage 2021;244.
[27] Pandelidis D, Anisimov S. Numerical analysis of the heat and mass transfer processes in selected M-Cycle heat exchangers for the dew point evaporative cooling. Energ Convers Manage 2015;90:62–83.
[28] Cui X, Chua KJ, Islam MR, Yang WM. Fundamental formulation of a modified LMTD method to study indirect evaporative heat exchangers. Energ Convers Manage 2014;88:372–81.
[29] Lin J, Bui DT, Wang R, Chua KJ. On the fundamental heat and mass transfer analysis of the counter-flow dew point evaporative cooler. Appl Energ 2018;217:126–42.
[30] Lin J, Bui DT, Wang R, Chua KJ. The counter-flow dew point evaporative cooler: Analyzing its transient and steady-state behavior. Appl Therm Eng 2018;143:34–47.
[31] Xu P, Ma X, Zhao X, Fancey K. Experimental investigation of a super performance dew point air cooler. Appl Energ 2017;203:761–77.
[32] Cui Y, Zhu J, Zoras S, Liu L. Review of the recent advances in dew point evaporative cooling technology: 3E (energy, economic and environmental) assessments. Renew Sustain Energy Rev 2021;148.
[33] Dizaji HS, Hu E, Chen L, Pourhedayat S, Wae-hayee M. Proposing the concept of mini Maisotsenko cycle cooler for electronic cooling purposes; experimental study. Case Stud Thermal Eng 2021;27.
[34] Liu Y, Yang X, Li J, Zhao X. Energy savings of hybrid dew-point evaporative cooler and micro-channel separated heat pipe cooling systems for computer data centers. Energy 2018;163:629–40.
[35] Khazhmuradov MA, Fedorchenko DV, Rudychev YV, Martynov S, Zakharchenko A, Prokhorets S, et al. Analysis of the Maisotsenko cycle based cooling system for accumulator batteries. Int J Energy Clean Environm 2011;12.
[36] Mahamud R, Park C. Reciprocating air flow for Li-ion battery thermal management to improve temperature uniformity. J Power Sources 2011;196:5685–96.
[37] Du X, Qian Z, Chen Z, Rao Z. Experimental investigation on mini-channel cooling-based thermal management for Li-ion battery module under different cooling schemes. Int J Energ Res 2018;42:2781–8.
[38] Zhao R, Zhang S, Liu J, Gu J. A review of thermal performance improving methods of lithium ion battery: Electrode modification and thermal management system. J Power Sources 2015;299:557–77.
[39] Tran T-H, Harmand S, Desmet B, Filangi S. Experimental investigation on the feasibility of heat pipe cooling for HEV/EV lithium-ion battery. Appl Therm Eng 2014;63:551–8.
[40] Ali M, Ahmad W, Sheikh NA, Ali H, Kousar R, Rashid Tu. Performance enhancement of a cross flow dew point indirect evaporative cooler with circular finned channel geometry. J Build Eng 2021;35.
[41] Fan X, Lu X, Nie H, Zhu H, Wang Q, Kang Y, et al. An experimental study of a novel dew point evaporative cooling tower based on M-cycle. Appl Therm Eng 2021;190.
[42] Lin J, Wang R, Li C, Wang S, Long J, Chua KJ. Towards a thermodynamically favorable dew point evaporative cooler via optimization. Energ Convers Manage 2020;203.
[43] Lin J, Chu HN, Monroe CW, Howey DA. Anisotropic thermal characterisation of largge-format lithium-ion pouch cells. Batteries & Supercaps 2022:e202100401.
[44] Chu HN, Kim SU, Rahimian SK, Siegel JB, Monroe CW. Parameterization of prismatic lithium–iron–phosphate cells through a streamlined thermal/electrochemical model. J Power Sources 2020;453:227787.
[45] Lin J, Wang RZ, Kumja M, Bui TD, Chua KJ. Multivariate scaling and dimensional analysis of the counter-flow dew point evaporative cooler. Energ Convers Manage 2017;150:172–87.
[46] Deng J, Bae C, Marcicki J, Masias A, Miller T. Safety modelling and testing of lithium-ion batteries in electrified vehicles. Nat Energy 2018;3:261–6.
[47] Jokar A, Rajabloo B, Désilets M, Lacroix M. Review of simplified Pseudo-two-Dimensional models of lithium-ion batteries. J Power Sources 2016;327:44–55.
[48] Yang X-G, Leng Y, Zhang G, Ge S, Wang C-Y. Modeling of lithium plating induced aging of lithium-ion batteries: Transition from linear to nonlinear aging. J Power Sources 2017;360:28–40.
[49] Wang Q-K, Shen J-N, Ma Z-F, He Y-J. Decoupling parameter estimation strategy based electrochemical-thermal coupled modeling method for large format lithium-ion batteries with internal temperature experimental validation. Chem Eng J 2021;424.
[50] Plett GL. Battery Management Systems: Battery Modeling. Artech House; 2015.
[51] Bernardi D, Pawlikowski E, Newman J. A general energy balance for battery systems. J Electrochem Soc 1985;132:5–12.
[52] Chen WD, Vivekh P, Liu MZ, Kumja M, Chua KJ. Energy improvement and performance prediction of desiccant coated dehumidifiers based on dimensional and scaling analysis. Appl Energ 2021;303.
[53] Lin J, Chu H, Howey D, Monroe C. Data repository for'Multiscale coupling of surface temperature with solid diffusion in large lithium-ion pouch cells'. University of Oxford; 2022.
[54] Lin J, Chu HN, Howey DA, Monroe CW. Multiscale coupling of surface temperature with solid diffusion in large lithium-ion pouch cells. Commun Eng 2022;1.
[55] Yang X-G, Liu T, Gao Y, Ge S, Leng Y, Wang D, et al. Asymmetric Temperature Modulation for Extreme Fast Charging of Lithium-Ion Batteries. Joule 2019;3:3002–19.
[56] Birkl CR, Roberts MR, McTurk E, Bruce PG, Howey DA. Degradation diagnostics for lithium ion cells. J Power Sources 2017;341:373–86.
[57] Zhu Y, Xie J, Pei A, Liu B, Wu Y, Lin D, et al. Fast lithium growth and short circuit induced by localized-temperature hotspots in lithium batteries. Nat Commun 2019;10:2067.